

ARTICLE TYPE

Local and Global Energies for Shape Analysis in Medical Imaging

Valerio Varano*¹ | Paolo Piras^{2,3} | Stefano Gabriele¹ | Luciano Teresi⁴ | Paola Nardinocchi³ | Ian L. Dryden⁵ | Concetta Torromeo² | Michele Schiariti² | Paolo E. Puddu²

¹Dipartimento di Architettura, Università Roma Tre, Italy

²Dipartimento di Scienze Cardiovascolari, Respiratorie, Nefrologiche, Anestesiologiche e Geriatriche, Università Sapienza, Italy

³Dipartimento di Ingegneria Strutturale e Geotecnica, Università Sapienza, Italy

⁴Dipartimento di Matematica e Fisica, Università Roma Tre, Italy

⁵School of Mathematical Sciences, University of Nottingham, UK

Correspondence

*Luciano Teresi. Email:

luciano.teresi@uniroma3.it

Summary

In a previous contribution a new Riemannian shape space, named TPS space, was introduced to perform statistics on shape data. This space was endowed with a Riemannian metric and a flat connection, with torsion, compatible with the given metric. This connection allows the definition of a Parallel Transport of the deformation compatible with the threefold decomposition in spherical, deviatoric and non affine components. Such a Parallel Transport also conserves the Γ -energy, strictly related to the total elastic strain energy stored by the body in the original deformation. New machinery is here presented in order to calculate the bending energy on the body only (body bending energy) in order to restrict it exclusively within physical boundaries of objects involved in the deformation analysis. The novelty of this new procedure resides in the fact that we propose a new metric to conserve during the TPS direct transport. This allows transporting the shape change more coherently with the mechanical meaning of the deformation. The geometry of the TPS Space is then further developed in order to better represent the relationship between the Γ -energy, the strain energy and the so called bending-energy densities.

KEYWORDS:

Shape analysis, bending energy, strain energy, parallel transport

1 | INTRODUCTION: SHAPE ANALYSIS IN CARDIAC IMAGING

Medical image analysis has experienced a significant boost in both shape recognition from medical images and analysis of related geometric data in the last two decades. In particular, 2D and 3D Speckle Tracking Echocardiography (2D and 3D STE), CT-scans and Magnetic Resonance (MR) imaging are commonly used in order to extract anatomical shapes from medical images to be analyzed and evaluated in terms of form, function and, ultimately, physiology. Shapes are identified by points (= landmarks) in 2D/3D space. These landmarks can be considered (with a certain degree of approximation) anatomically homologous or not between different subjects. In the former case anatomical homology allows the possibility of analysing landmarks with the standard Geometric Morphometrics (GM) toolkit successfully applied in a wide range of disciplines from paleobiology (^{1,2,3}) to medicine (⁴).

Without the homology assumption several strategies have been developed in order to perform shape matching basing on a plethora of algorithms (^{5,6}) whose review is not the scope of the present paper. In recent years the emerging disciplines of Diffeomorphometry and the related Functional Anatomy have been applied to supplement classic GM through the use of diffeomorphisms, which are more suitable to describe soft tissues changes (^{7,8,9}). On the other hand, these descriptions are very sophisticated but do not incorporate in their formulation some synthetic properties of the decomposition of deformation in some

significant aspects. In this paper we focus on shapes represented by landmarks that are considered anatomically homologous in different configurations. Very often, in medical applications, the goal of shape analysis is not the assessment of differences between shapes; rather, the main aim is to find differences between deformations. This distinction is crucial and inevitably leads to the definition and quantification of deformation occurring between two shapes, e.g. a source and a target^(10,11,4). In this paper we focus our attention on the Left Ventricle (LV) cardiac revolution represented by 2D shapes deriving from projections on the coronal plane of the whole LV 3D reconstruction coming from 3D Speckle Tracking Echocardiography (3DSTE). In particular, we present a theoretical framework that suggests an efficient method for calculating the body bending energy and the Γ -energy observed in a generic deformation. In the present paper the formulation of the TPS Space^(12,13) is further developed in order to better represent the relationship between the Γ -energy, the strain energy and the so called bending-energy densities. The bending energy is then calculated on the body only (body bending energy) in order to restrict it exclusively within the physical boundaries of objects involved in the deformation analysis. The utility of these quantities is illustrated by an application of the TPS Direct Transport^(12,13) to two LV belonging to one healthy and one pathological individual affected by Hypertrophic Cardiomyopathy. The use of only two individuals here is purely didactic thus without clinical significance and exclusively aimed at showing the important implications of energy density conservation instead of absolute energy. For computational reasons we present here a formulation applicable only to 2D cases. However, a 3D generalization can be achieved by further exploring the potential of integration techniques on the surface boundaries.

2 | DEFORMATIONS IN SIZE AND SHAPE SPACE

In landmark based Geometric Morphometrics, configurations are represented by $k \times m$ matrices, where k is the number of landmarks and m the dimension of the Euclidean ambient space \mathcal{E}^m , identified with \mathbb{R}^m and endowed with an orthonormal basis e_1, \dots, e_m fixed once for all. The positions $x \in \mathcal{E}^m$ of k points, called *landmarks*, define a *configuration* of the body, which can be represented as a $k \times m$ matrix $X = (x_1, \dots, x_k)^T$, where $x_i = (x_{i1}, \dots, x_{im})^T$ are the coordinates of the i -th landmark with respect to e_1, \dots, e_m ⁽¹⁴⁾.

When configurations are centered, a strict representation is given by $(k-1) \times m$ matrices. The space of each centered configuration, the so-called *Centered Configuration Space* CC_m^k can be identified with the linear space of the $(k-1) \times m$ matrices. On each point $X \in CC_m^k$, representing a configuration, the tangent space $\mathcal{T}_X CC_m^k$ is defined. A vector $V \in \mathcal{T}_X CC_m^k$ represents a small deformation of the configuration X and can be represented, in turn, by a $(k-1) \times m$ matrix.

We define the *centered configuration* X_C as the $k \times m$ matrix:

$$X_C = CX$$

where $C = I_k - \frac{1}{k} \mathbf{1}_k \mathbf{1}_k^T$, I_k is the $k \times k$ identity matrix and $\mathbf{1}_k$ is a $k \times 1$ column of ones.

We define the *Helmertized configuration* X_H as the $(k-1) \times m$ matrix:

$$X_H = HX$$

where H is the so called Helmert sub-matrix. The j -th row of the Helmert sub-matrix H is given by

$$(h_j, \dots, h_j, -jh_j, 0, \dots, 0), \quad h_j = -(j(j+1))^{-1/2}$$

and so the j -th row consists of h_j repeated j times, followed by jh_j and then $k-j-1$ zeros, $j = 1, \dots, k-1$. One can switch from one parametrization to the other by using the properties:

$$H^T H = C,$$

and then

$$X_C = H^T X_H, \quad X_H = H X_C.$$

If one wants to filter out every rigid motion then rotations are removed, thus obtaining the *size-and-shape space* $S\Sigma_m^k = CC_m^k/SO(m)$ as a quotient space with respect to the rotation group.

If one wants to filter out the scaling too, then each *form* is scaled to unit *size*, thus obtaining the *shape space* Σ_m^k . This is the reason upon which the geometry of the shape space depends on the choice of a size measure. This choice is not obvious.

In order to describe and compare different deformations it is very important to be able to decompose each deformation by projecting it on different subspaces of $\mathcal{T}_X CC_m^k$, each one characterizing some important features of the deformation.

In order to describe the deformation it is important to introduce some important subsets of $\mathcal{T}_X(CC_m^k)$, introduced in¹³.

The first is the set \mathcal{V}_u of the uniform deformations of X :

$$\mathcal{V}_u = \{V \in \mathcal{T}_X(CC_m^k) : V = XA^T, A \in GL(m)\}, \quad (2.1)$$

It describes the overall deformation of the reference configuration.

There are other two very important subspaces that are, in turn, subspaces of \mathcal{V}_u : the *spherical* (homothetic) deformations of X $\mathcal{V}_{sph} \subset \mathcal{V}_u$ and the *small rotations* of X $\mathcal{V}_{rot} \subset \mathcal{V}_u$:

$$\mathcal{V}_{sph} = \{V \in \mathcal{T}_X(CC_m^k) : V = \lambda X, \lambda \in \mathbb{R}\} \quad (2.2)$$

$$\mathcal{V}_{rot} = \{V \in \mathcal{T}_X(CC_m^k) : V = XW, W \in C_m^m, W + W^T = 0\}. \quad (2.3)$$

While each one of the above mentioned subspaces has a direct characterization, there are two important subspaces, namely the set \mathcal{V}_{nu} of the non-uniform deformations of X , and the set \mathcal{V}_{nsph} of the non-spherical deformations of X , that admit only indirect definitions, as orthogonal complements. In particular:

$$\mathcal{V}_{nu} = \{V \in \mathcal{T}_X(CC_m^k) : g(U, V) = 0 \forall U \in \mathcal{V}_u\} \quad (2.4)$$

$$\mathcal{V}_{nsph} = \{V \in \mathcal{T}_X(CC_m^k) : g(U, V) = 0 \forall U \in \mathcal{V}_{sph}\}. \quad (2.5)$$

In such a way the following decompositions holds:

$$\mathcal{T}_X(CC_m^k) = \mathcal{V}_u \oplus^g \mathcal{V}_{nu} = \mathcal{V}_{sph} \oplus^g \mathcal{V}_{nsph} \quad (2.6)$$

where \oplus^g is the orthogonal sum *with respect to the metric tensor g* . In fact the *orthogonality* is not a concept given a priori but it is defined by the metric tensor. We want to stress that g depends on the considered point X then the *orthogonality* depends on X .

By defining the *deviatoric* component as the *uniform non spherical* component:

$$\mathcal{V}_{dev} = \mathcal{V}_{nsph} \cap \mathcal{V}_u \quad (2.7)$$

we obtain, in turn, the following orthogonal decomposition, w.r.t. g , on each configuration X :

$$\mathcal{T}_X(CC_m^k) = \underbrace{\mathcal{V}_{rot} \oplus^g \overbrace{\mathcal{V}_{sph} \oplus^g \mathcal{V}_{dev}}^{\mathcal{V}_{nsph}} \oplus^g \mathcal{V}_{nu}}_{\mathcal{V}_u} \quad (2.8)$$

It is easy to understand that the above decomposition can be interpreted as a splitting of the (small) deformation in a component that changes only *orientation, size, shape*.

$$\mathcal{T}_X(CC_m^k) = \underbrace{\mathcal{V}_{rot}}_{orientation} \oplus^g \underbrace{\overbrace{\mathcal{V}_{sph} \oplus^g \mathcal{V}_{dev} \oplus^g \mathcal{V}_{nu}}^{form}}_{size \quad shape} \quad (2.9)$$

Then, given a small deformation V_X of the configuration X , the rotational component V_{rot} must be filtered out by using a proper procedure of alignment (either Ordinary Procrustes Analysis (OPA) or Modified Ordinary Procrustes Analysis (MOPA) see below).

If one performs the quotient with respect to the rotation group, for obtaining the *size-and-shape space* $S\Sigma_m^k = CC_m^k/SO(m)$, the above decomposition can be interpreted as a decomposition in *vertical subspace* (\mathcal{V}_{rot}) and *horizontal subspace* (the orthogonal complement $\mathcal{V}_{sph} \oplus^g \mathcal{V}_{dev} \oplus^g \mathcal{V}_{nu}$). The horizontal subspace on the configuration X represents (is isometric to) the tangent space to the size-and-shape space $S\Sigma_m^k$ at the *form* $[X]_S$, where $[X]_S$ is the equivalence class given by the action of $SO(m)$ on X .

It is important to stress that the above decomposition, in general, relies on the choice of g . In the next sections we will introduce, as g , the so called TPS metric (¹²).

3 | GEOMETRY OF THE TPS SPACE

3.1 | Thin Plate Spline

By following the notation of^{14,12} we summarize the construction of the Thin Plate Spline (TPS), and we refer to^{15,14,12} for further details. In the Euclidean space \mathcal{E}^m , the m -tuple of interpolating TPS is a function Φ represented by the pair (A_X, W_X) , where: A_X is a linear transformation of \mathcal{E}^m , represented by a $(m \times m)$ matrix and W_X is a $(k \times m)$ matrix. Given a point $x \in \mathcal{E}^m$, and a centred configuration $X \in CC_m^k$, we have

$$x' = \phi(x) = A_X x + W_X^T s(x), \quad (3.10)$$

where $s(x) = (\sigma(x - x_1), \dots, \sigma(x - x_k))^T$ is a $(k \times 1)$ matrix, $x_i \in X$ is the position of the i -th landmark, and

$$\sigma(h) = \begin{cases} \|h\|^2 \log(\|h\|^2) & \text{if } \|h\| > 0; \\ 0 & \text{if } \|h\| = 0. \end{cases} \quad \text{for } m = 2$$

$$\sigma(h) = \begin{cases} -\|h\| & \text{if } \|h\| > 0; \\ 0 & \text{if } \|h\| = 0. \end{cases} \quad \text{for } m = 3$$

Given a *undeformed configuration* X , and a *deformed configuration* X' , we can apply equation (3.10) landmark-wise, yielding to

$$X' = X A_X^T + S_X W_X, \quad \text{with } (S_X)_{ij} = \sigma(x_i - x_j). \quad (3.11)$$

There are $2k$ interpolation constraints in equation (3.11), and we introduce $m \times (m + 1)$ more constraints on W in order to uncouple the affine and non affine parts:

$$1_k^T W_X = 0, \quad X^T W_X = 0. \quad (3.12)$$

For a given pair (X, Y) there exists a unique set of parameters for the pair (A_X, W_X) that solve the problem (3.11), constrained with (3.12):

$$A_X^T = \Gamma_{21X} X', \quad W_X = \Gamma_{11X} X', \quad (3.13)$$

where

$$\begin{aligned} \Gamma_{21X} &= (X^T S_X^{-1} X)^{-1} X^T S_X^{-1} \\ \Gamma_{11X} &= S_X^{-1} - S_X^{-1} X \Gamma_{21X} \end{aligned}$$

are a $m \times (k - 1)$ and a $(k - 1) \times (k - 1)$ matrices, respectively, which only depend on the source configuration X .

Finally the target X' can be represented as the deformation of X :

$$X' = X \Gamma_{21X} X' + S_X \Gamma_{11X} X' = X A_X^T + S_X W_X. \quad (3.14)$$

The centred coordinates can be recovered simply by pre-multiplying with H^T . The matrix $(k - 1) \times (k - 1)$ matrix Γ_{11X} is called *Bending Energy matrix* and represents the non linear part of the deformation. Because it vanishes on linear deformations, its eigenvectors associated to non vanishing eigenvalues are only $(k - 1 - m)$. They are called *principal warps* and represent the principal modes of deformation.^{14,12}

3.2 | Strain Energy (SE), Bending Energy (BE), Body Bending Energy (BEB)

One of the main features of the TPS method is that it minimizes the so called *bending energy* J , involving the second derivative of the displacements¹⁵. In particular, given a body, represented in the undeformed configuration, by the regular region Ω of \mathbb{R}^m , we label x the points in Ω and x' the points in the deformed configuration Ω_t at the instant t . If the configurations are sampled in k landmarks, then Ω can be represented by the $k \times m$ matrix X and Ω_t by the deformed configuration X . The displacement field is represented by the difference vectors:

$$u(x) = x' - x \quad (3.15)$$

In the landmark case the displacements experienced by the k landmarks can be collected in the $k \times m$ matrix $U = Y - X$.

The bending energy is defined as:

$$J = \int_{\mathbb{R}^m} \nabla^2 u \cdot \nabla^2 u \quad (3.16)$$

Note that the bending energy is defined as an integral on the whole \mathbb{R}^m , which does not diverge because the curvature of the TPS, outside of Ω , decays quickly to zero ⁽¹⁶⁾.

The bending energy can be considered as a pseudo-metric on \mathcal{TCC}_m^k because it measures the difference between two configurations but it vanishes on the affine deformations.

A nonsingular distance, used in the deformable templates method ¹⁷, is the Dirichlet Energy φ_D .

$$\varphi_D = \frac{1}{2} \int_{\Omega} \nabla u \cdot \nabla u \quad (3.17)$$

A more physical distance, used in continuum mechanics, that vanishes on the rotational part of the local deformation, is the *complete strain energy* φ_S

$$\varphi_S = \frac{1}{2} \int_{\Omega} 2\mu E \cdot E + \lambda(\text{tr}E)^2 \quad (3.18)$$

where μ, λ are the Lamé elastic moduli, related to the material properties of the body, and

$$E = \frac{\nabla u + (\nabla u)^T}{2} \quad (3.19)$$

is the strain tensor (in the case of small displacements). Here, because we are describing only geometrical features, we assume a simplified expression for the *strain energy* φ :

$$\varphi = \frac{1}{2} \int_{\Omega} E \cdot E \quad (3.20)$$

In ⁽¹³⁾, in order to give a physical interpretation of the bending energy, the *body-bending energy* has been introduced, performing the integration only on the body:

$$J_{\Omega} = \int_{\Omega} \nabla^2 u \cdot \nabla^2 u \quad (3.21)$$

In general the bending energy will be slightly greater than the body-bending energy and the *decay* $\rho = J/J_{\Omega}$ can be used to quantify this difference.

In ⁽¹³⁾ has been shown that, for bilinear deformations in 2D, in which a rectangle bends in a trapezoid:

$$u = [(\chi \otimes e_1 \otimes e_2) x]x \quad (3.22)$$

where $\chi = \chi_1 e_1 + \chi_2 e_2$ are the bending with respect to the two axes, the strain energy is directly proportional to the body-bending energy and the proportionality coefficient depends only on geometrical quantities of Ω .

In particular the following relationship holds:

$$\varphi = \frac{I_p}{4\mathcal{A}} J_{\Omega} \quad (3.23)$$

where I_p and \mathcal{A} are the polar inertia and the area of Ω , respectively.

On the other hand for a uniform deformation, such that $x' = Ax$, and A is a $(m \times m)$ matrix, it is clear that the strain energy is directly proportional to the square of the Frobenius norm of $(A - I)$:

$$\varphi = \frac{1}{2} \mathcal{A}(A - I) \cdot (A - I) \quad (3.24)$$

where I is the $(m \times m)$ identity matrix.

A general bilinear deformation can be parametrized as follows:

$$u = (A - I)x + [(\chi \otimes e_1 \otimes e_2) x]x \quad (3.25)$$

3.3 | BE matrix and BEB matrix

An interesting and useful feature of the TPS is that the value of the bending energy J associated to a deformation U of a configuration X is directly proportional to the quadratic form $\text{Tr}(U^T \Gamma_{11X} U)$

$$J(U) \propto \text{Tr}(U^T B U). \quad (3.26)$$

For this reason the matrix $B := \Gamma_{11X}$ is also called Bending Energy Matrix of X . In fact one of the most important reasons of the success of the TPS is the possibility to evaluate the BE directly by means of a closed form expression, avoiding the need to discretize the configuration in a huge number of triangles. Furthermore the BE matrix depends only on the undeformed configuration and can be used as pseudo-metric on \mathcal{TCC}_m^k .

We show here that also for the body-bending energy calculation, it is possible to define a symmetric matrix B_Ω , such that holds:

$$J_\Omega(U) \propto \text{Tr}(U^T B_\Omega U) \quad (3.27)$$

Then the decay $\rho(U)$ can be calculated by means of the Rayleigh quotient:

$$\rho(U) = \frac{J(U)}{J_\Omega(U)} = \frac{\text{Tr}(U^T B U)}{\text{Tr}(U^T B_\Omega U)} \quad (3.28)$$

whose extreme values result from the solution of the generalized eigenvalue problem $\text{Eig}(B, B_\Omega)$. In the particular case in which BEB and BE matrices commute (i.e. $[B, B_\Omega] = B B_\Omega - B_\Omega B = 0$) the decay assumes the same value for each deformation mode.

In order to build the BEB matrix we follow, using a different notation, the procedure described in (16). In the following, for the sake of simplicity, we limit ourselves to consider 2D configurations, defined by landmarks on the boundary of the body and in the interior (Figure 1).

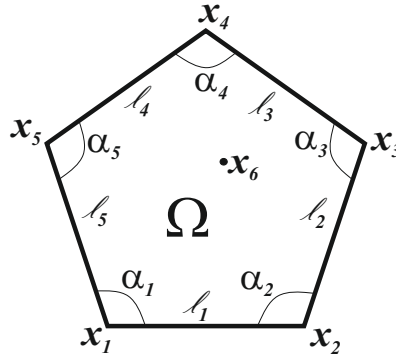


FIGURE 1 Example of 2D configuration, made by 6 landmarks, the firsts 5 lying on the boundary and one, x_6 , inside the region Ω .

The whole procedure is based on the following property of the biharmonic function σ :

$$\Delta^2 \sigma(x) = 16\pi \delta_o(x) \quad (3.29)$$

where δ_o is the Dirac function, defined as the generalized function such that:

$$\int_{\mathbb{R}^n} \delta_o(x) f(x) = f(0) \quad (3.30)$$

As explained in the previous sections, once performed a TPS on two configurations X and $X' = X + U$ we can describe the deformation as:

$$\phi(x) = A_X x + W_X^T s(x), \quad (3.31)$$

In order to calculate the BEB we take the second gradient thus obtaining:

$$\nabla^2 \phi(x) = W_X^T \nabla^2 s(x), \quad (3.32)$$

The BEB can be then calculated by the following integral:

$$\begin{aligned} J_{\Omega}(U) &= \int_{\Omega} \nabla^2 \phi \cdot \nabla^2 \phi = \int_{\Omega} (W_X^T \nabla^2 s(x) \cdot W_X^T \nabla^2 s(x)) = \int_{\Omega} \text{Tr} (W_X^T \nabla^2 s(x) (\nabla^2 s(x))^T W_X) \\ &= \text{Tr} \left(W_X^T \int_{\Omega} \nabla^2 s(x) (\nabla^2 s(x))^T W_X \right) = \text{Tr} \left(X'^T \Gamma_{11X} \int_{\Omega} \nabla^2 s(x) (\nabla^2 s(x))^T \Gamma_{11X} X' \right) \\ &= \text{Tr} (X'^T B_{\Omega} X') = \text{Tr} ((X + U)^T B_{\Omega} (X + U)) = \text{Tr} (U^T B_{\Omega} U) \end{aligned} \quad (3.33)$$

where the BEB matrix is then defined as follows:

$$B_{\Omega} := \Gamma_{11X} \left(\int_{\Omega} \nabla^2 s(x) (\nabla^2 s(x))^T \right) \Gamma_{11X} = \Gamma_{11X} C \Gamma_{11X} \quad (3.34)$$

In order to calculate the component of the matrix we integrate by parts:

$$\begin{aligned} C_{ij} &= \left(\int_{\Omega} \nabla^2 s(x) (\nabla^2 s(x))^T \right)_{ij} = \int_{\Omega} \nabla^2 s_i(x) \cdot \nabla^2 s_j(x) \\ &= \int_{\Omega} \Delta^2 s_i(x) s_j(x) + \int_{\partial\Omega} (\nabla^2 s_i(x) \nabla s_j(x) - s_i(x) \text{div} (\nabla^2 s_j(x))) \cdot \mathbf{n} \end{aligned}$$

where \mathbf{n} is the outer unit normal vector field to the boundary. Then, by using eq. (3.29) and (3.30) we obtain, for the bulk term of the integral:

$$(C_{\Omega})_{ij} = \int_{\Omega} \Delta^2 s_i(x) s_j(x) = \int_{\Omega} \delta_{\alpha}(x - x_i) \sigma(x - x_j) = \frac{32\pi^2}{\alpha_i} \sigma(x_i - x_j) \quad (3.35)$$

where the values of the angles α_i , taking into account the integration of the Dirac delta on Ω instead of \mathbb{R}^2 , depend on the position of the i -th landmark with respect to Ω , in particular:

$$\alpha_i = \begin{cases} 2\pi & \text{if } x_i \in \Omega; \\ \arccos\left(\frac{\ell_i}{\|\ell_i\|} \cdot \frac{\ell_{i+1}}{\|\ell_{i+1}\|}\right) & \text{if } x_i \in \partial\Omega. \end{cases} \quad (3.36)$$

where $\ell_i = (x_{i+1} - x_i)$ (see Fig. 1).

For the boundary term we obtain:

$$\begin{aligned} (C_{\partial\Omega})_{ij} &= \int_{\partial\Omega} (\nabla^2 s_i(x) \nabla s_j(x) - s_i(x) \text{div} (\nabla^2 s_j(x))) \cdot \mathbf{n} = \sum_{p=1}^{k-q} \int_{\partial\Omega_k} (\nabla^2 s_i(x) \nabla s_j(x) - s_i(x) \text{div} (\nabla^2 s_j(x))) \cdot \mathbf{n}_p \\ &= \sum_{p=1}^{k-q} \int_0^1 (\nabla^2 s_i(x_p + \zeta \ell_p) \nabla s_j(x_p + \zeta \ell_p) - s_i(x_p + \zeta \ell_p) \text{div} (\nabla^2 s_j(x_p + \zeta \ell_p))) \cdot * (\ell_p) d\zeta \end{aligned} \quad (3.37)$$

Where the p -th side of Ω is represented by $x_p + \zeta \ell_p$, \mathbf{n}_p is the unit normal to the p -th side, $* (\ell_p)$ is the vector ℓ_p rotated clockwise by $\pi/2$. We note that q is the number of landmarks that does not lie on the boundary $\partial\Omega$, while $(k - p)$ is the number of landmarks lying on $\partial\Omega$.

Finally, we can put together each term:

$$B_{\Omega} = \Gamma_{11X} C_{\Omega} \Gamma_{11X} + \Gamma_{11X} C_{\partial\Omega} \Gamma_{11X} \quad (3.38)$$

It is possible to prove (see¹⁶ for the proof) that, fixing the landmarks and changing the integration domain, in such a way that $\Omega \rightarrow \mathbb{R}^2$, then $B_{\Omega} \rightarrow 16\pi B$. This can be qualitatively understood by considering that, in that case the boundary term $C_{\partial\Omega}$ vanishes and, for the bulk term C_{Ω} , there are no landmarks belonging to $\partial\Omega$ and then $\alpha_i = 2\pi$ for each i , and by using the notable property $\Gamma_{11X} S_X \Gamma_{11X} = \Gamma_{11X}$ (^{12,13}). It is important to stress that, for $\Omega \subset \mathbb{R}^2$ the bulk term C_{Ω} has the closed form representation (3.35), while the boundary term $C_{\partial\Omega}$ is calculated solving, numerically, the single variable integrals appearing in Eq. (3.37), that involve the derivatives of the biharmonic function. The BEB matrix computation is here presented only for 2D data because the procedure of integration by parts in that case leads to a line integration that can be easily performed. In

the 3D case equations (3.35)-(3.37) should become much more complicated. However, a 3D generalization can be achieved by numerical integration techniques on a surface's boundaries.

3.4 | TPS Metric and Γ -Energy

In this section we introduce a modified expression for the TPS metric formulated in ⁽¹²⁾ and discussed in ⁽¹³⁾. This modification is motivated by two reasons: the introduction of the BEB matrix, and the consideration that the best quantity to conserve in a parallel transport of deformation is not the *total strain energy* but the *mean strain energy density*. Let consider two bodies having the same shape but a different size (volume), undergoing the same deformation, for example a global stretching of 30%, storing different quantities of strain energy, but the same average strain energy.

Then, we propose a general representation for the metric tensor:

$$g(U, V) := \text{Tr}(U^T G V) \quad (3.39)$$

where

$$G := \mu_1 \Gamma_{21X}^T \Gamma_{21X} + \mu_2 B_\Omega = G_u + G_{nu} \quad \mu_1 = \frac{1}{2} \text{ and } \mu_2 = \frac{I_p}{4A^2} \quad (3.40)$$

It is important to stress that Γ_{21X} , B_Ω , μ_2 depend on the source configuration X . Let given two configurations X and $X' = X + U$, by means of the introduced metric, we can define the distance between X and X' called Γ -Energy, as follows:

$$\Gamma(X, X') := g((X' - X), (X' - X)) = \text{Tr}((X' - X)^T G (X' - X)) \quad (3.41)$$

We could consider the Γ -energy $\Gamma(U)$ as the average strain energy $\varphi(\tilde{U})$ evaluated on a more simple deformation \tilde{U} characterized by the same uniform component $\tilde{U}_u = U_u$ of U and a bilinear deformation \tilde{U}_{nu} storing the same body bending energy of U_{nu} , i.e. such that $J_\Omega(\tilde{U}_{nu}) = J_\Omega(U_{nu})$.

3.4.1 | Filtering rotations: OPA and MOPA

Once introduced the TPS metric tensor G , a general technique of between two forms $[X]_S$ and $[Y]_S$ is based on the minimization of the distance defined as:

$$d([X]_S, [Y]_S) = \inf_{Q \in SO_m} \sqrt{\text{Tr}((YQ - X)^T G^\alpha (YQ - X))}.$$

The *aligned configuration* \hat{Y} is obtained by means of an *optimal rotation* \hat{Q} minimizing d .

$$\hat{Y} = Y \hat{Q}$$

where $\hat{Q} = \text{argmin}_Q g((YQ - X), (YQ - X))$. According to this definition, \hat{Q} turns out to be the rotational component of the polar decomposition of $Y^T G X$.

When $\alpha = 0$ we obtain the rotational component of $Y^T X$ (the classical Ordinary Procrustes Analysis (OPA)¹⁴). When $\alpha = 1$ then $Y^T G X = A_X$. In the latter case we define the alignment Modified OPA (MOPA)¹².

3.5 | TPS Direct Transport

In ⁽¹²⁾ a connection named TPS connection was introduced. It has the following properties:

1. It is compatible with the TPS metric,
2. It is compatible with the decomposition given in (2.9),
3. It preserves the Γ -energy,
4. It is independent of the path.

In this section we reformulate this Parallel Transport procedure by implementing it with a new feature that takes in consideration the physical boundaries of the bodies involved. We also assume all the configurations to be centred, and represented by the

Helmertized landmarks, then, if not otherwise specified, each matrix is a $(k - 1) \times m$ matrix. Furthermore deformation vectors will have a subscript denoting the starting point, that is, the source configuration (for details see¹²).

Let X and Y be two source configurations, and V_X, V_Y the two associated deformation vectors, given by:

$$\begin{aligned} V_X &= X' - X = X(A_X^T - I) + S_X W_X, \\ V_Y &= Y' - Y = Y(A_Y^T - I) + S_Y W_Y. \end{aligned} \quad (3.42)$$

We say that V_Y is the parallel transport of a given V_X , that is, $V_Y = \tau_{Y,X}(V_X)$, if and only if the uniform part of V_Y equals that of V_X :

$$A_Y = A_X;$$

and the non uniform part W_Y of V_Y solves the linear systems:

$$Y^T W_Y = X^T W_X = 0 \quad Q_Y E_Y^T W_Y = Q_X E_X^T W_X, \quad (3.43)$$

where the $(k - 1) \times (k - 1 - m)$ *body principal warps matrix* E_X , collects all the body principal warps of X , while Q_X is a suitable $(k - 1 - m) \times (k - 1 - m)$ orthogonal matrix (i.e. $Q_X^T Q_X = I$), defined on each configuration X , representing a rotation, or a reflection, of the principal warps. Once chosen a configuration P as a Pole for the space, Q_X is estimated minimising the Euclidean distance $\|E_X Q_X^B - E_P\|$ between the rotated principal warps of X , and the corresponding basis on the pole P .

The first equation of (3.43) constrains W_b to be orthogonal to the affine part, while the second define the isometry in the subspace of the non affine deformations. This last requirement implies the conservation of the total bending energy. The system (3.43) can be written as:

$$\begin{bmatrix} Y^T \\ Q_Y E_Y^T \end{bmatrix} [W_Y] = \begin{bmatrix} X^T \\ Q_X E_X^T \end{bmatrix} [W_X].$$

That can be re-written as:

$$W_Y = M_Y^{-1} M_X W_X$$

And so:

$$V_Y = (Y \Gamma_{21X} + S_Y M_Y^{-1} M_X \Gamma_{11X}) V_X, \quad (3.44)$$

The equation (3.44) characterizes V_Y as the parallel transport of V_X .

The only difference between the original TPS Direct Transport (¹²) and that introduced here is in the definition of the $(k - 1) \times (k - 1 - m)$ matrix E_X , collecting, here, all the *body principal warps* of X in columns. Then we call it the *body principal warps matrix*. We can build it as follows:

- Perform a TPS analysis on X and find the BEB matrix B_Ω (eq. 3.38),
- Perform an eigenvalue analysis on B_Ω and obtain $B_\Omega = \Gamma \Lambda \Gamma^T$ where Γ is the $(k - 1) \times (k - 1)$ matrix containing, in column, the eigenvectors γ_i , and Λ is the diagonal $(k - 1) \times (k - 1)$ matrix of the eigenvalues $\lambda_1, \dots, \lambda_{k-1}$, ordered by increasing magnitude. The first m eigenvalues will be equal to 0,
- Drop the first m columns from Γ , by obtaining the $(k - 1) \times (k - 1 - m)$ matrix $\bar{\Gamma}$, containing the *body principal warp* eigenvectors by column,
- Drop the first m rows and the first m columns from Λ , by obtaining the $(k - 1 - m) \times (k - 1 - m)$ matrix $\bar{\Lambda}$,
- Define the $(k - 1) \times (k - 1 - m)$ matrix $E_X = S_X \bar{\Gamma} \bar{\Lambda}^{1/2}$

The same steps must be used to build the *body principal warps matrix* E_Y on the target configuration.

All the above mentioned formulations have been implemented in R by using ad hoc built and easy to use R functions available from the authors upon request.

4 | CARDIAC EXAMPLES

We tested our procedure on real data coming from 3D Speckle-Tracking- Echocardiography (3D-STE) of human left ventricles (LV). In order to illustrate the approaches we describe here, we contrasted two complete cycles relative to 1 healthy subjects

and 1 to a patient affected by hypertrophic cardiomyopathy. The use of only two individuals here is purely didactic thus without clinical significance and exclusively aimed at showing the profound implications of the body energy density conservation instead of total bending energy. These data come from the same research project partially published in (^{18,19,20,21,22,23,24}), and have been collected by means of 3D-STE (PST25SX Artida, Toshiba Medical Systems Corp., Tokyo, Japan). The whole LV geometry is reconstructed by starting from a set of 6 homologous landmarks, manually detected by the operator for each subject under study. The manual detection of the initial set of landmarks is crucial to fulfil a homology principle, so that comparable anatomical structures of different subjects are detected; completely automated approaches may suffer from error of pattern identification depending on the specific algorithm used for reconstruction. The data set generated for each subject by 3D-STE consists of a sequence of 3D configurations, acquired every 45 ms, each constituted by 1297 landmarks, assumed to be homologous, for both the epicardial and endocardial surfaces, positioned along 36 horizontal circles, each comprised of 36 landmarks, plus the apex (Fig. 2 left). After the generation of the data set, we define 16 time-events according to (¹⁸), to be used as homologous times to sample the heart beating (using cubic spline interpolation) for both subjects as shown in Fig. 3, and we assemble a trajectory for each subject by extracting from the data set a sequence of 32 configurations corresponding to the homologous time-events (¹⁸). Finally, in order to present our results in 2-dimensions, for each trajectory, we project a coronal slice of the 3D configurations (interpolated at homologous times) on the plane transversal to the LV base, identified by three points on the epicardium: the LV apex, the point lying on the mitral annulus in correspondence on the middle of the interventricular septum and that lying on the opposite lateral side (Fig. 2 right); this plane is selected at the first homologous time, i.e. at the R peak (=telediastole) and all shapes corresponding to other times were projected on that plane. This allows to better conserve, during projection, the torsional movement of the LV for the duration of the cycle. Our procedure entirely mimics the 2D-speckle tracking (2DSTE) approach except for the lesser time' resolution. However this does not affect our result's interpretation given the methodological aim of the present contribution.

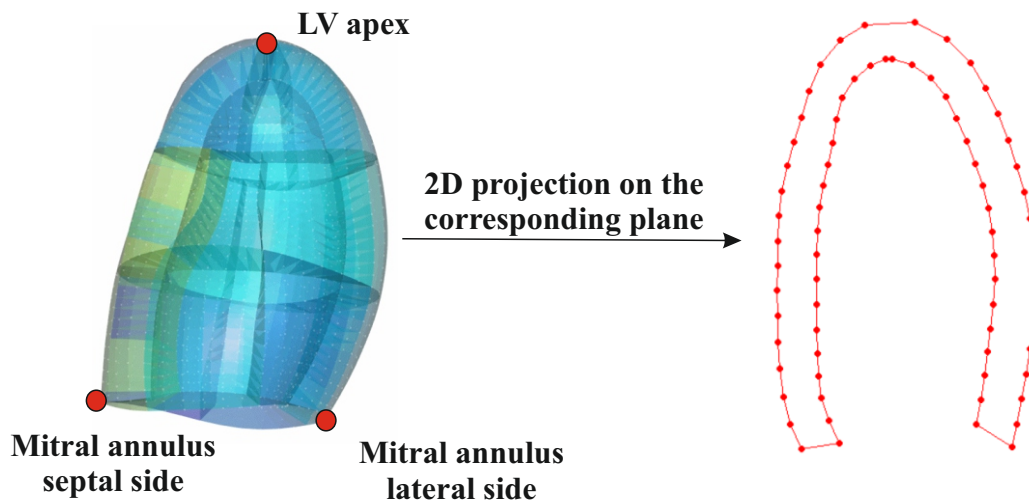


FIGURE 2 3D data coming from PST25SX Artida echocardiographic device with the triplet of landmarks used for projection (Left) on the coronal plane (Right).

4.1 | Bilinear deformations of a vertical cross section of a LV

A simulated dataset (Fig. 4) was generated by deforming, parametrically, the diastolic state of the healthy individual through bilinear deformations (Eq.3.25). Deformations were built using 6 parameters, A_{11} , A_{12} , A_{21} , A_{22} , χ_1 , χ_2 each following 6 series of thirty randomly chosen values, and successively sorted in ascending order, in a uniform distributions evaluated in the intervals $A_{11} \in [-0.2, 1.2]$, $A_{12} \in [-0.2, 1.2]$, $A_{21} \in [-0.02, 0.12]$, $A_{22} \in [0, 0.01]$, $\chi_1 \in [0, 0.01]$, $\chi_2 \in [0, 0.01]$ respectively. The diastolic state was chosen as the source configuration (=the undeformed shape) while the 30 deformed shapes were the targets. We then computed the body bending energy matrix on the source and we used it in order to compute the body bending energy

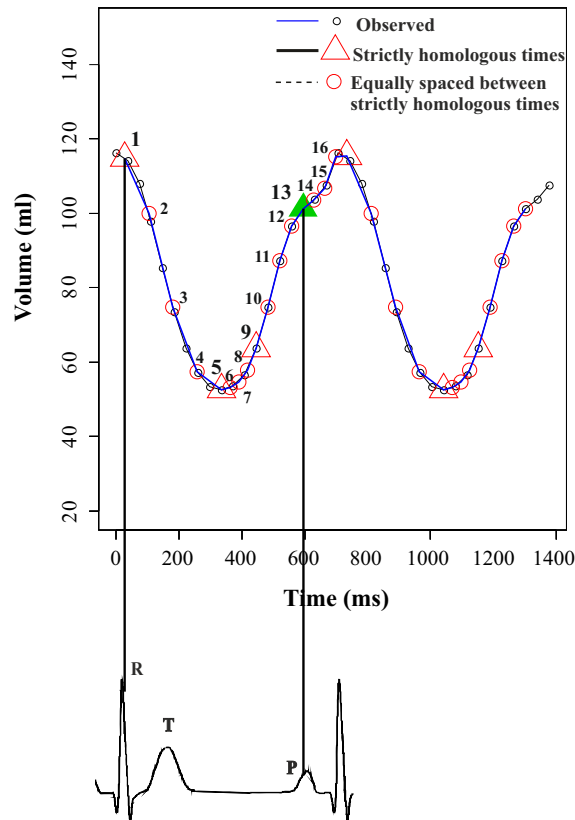


FIGURE 3 Before projection 3D data were interpolated at homologous times according to homologous electro-mechanical events. As univariate example we show here the interpolation (using cubic spline) of Volume values for one individual.

and the gamma energy according to (3.33) and (3.41). We also computed the strain energy and the bending energy according to (3.20) and (3.16).

4.2 | Deformations of a set of vertical cross sections of acquired LVs

We used the two cycles in order to proceed with an implemented version of the TPS Direct Transport procedure described in¹². We chose the consensus of the all 32 shapes enlarged 5 times (in order to generalize the procedure by considering also a large size difference) as the Common Reference (CR) toward which per-cycle deformations, estimated from per-cycle local references (LOCS), were transported. We chose as LOCS the two consensus of each individual cycle. In order to achieve this we computed the body bending energy matrices of CR and LOCS as well as $\mu_1\text{CR}$, $\mu_2\text{CR}$, $\mu_1\text{LOCS}$ vector (two values in this case as we have two LOCS) and $\mu_2\text{LOCS}$ vector (two values). We then contrasted the Energy densities computed after the TPS Direct Transport procedure between the Common Reference and transported data contrasted with the Energy densities calculated on original data between LOCS and their proper deformed states. We expect isometry for both body bending energy density and gamma energy density while it is not expected for strain energy density and bending energy density.

5 | RESULTS

Fig. 5 left shows that the Strain Energy is very close to the Γ -Energy in the simulated example (β coefficient: 1.14); in particular, at the beginning of the deformations series their relationship is very close to isometry while it is not exactly the case for larger deformations. This could be due to the triangulation' discretization during Strain Energy calculation. Fig. 5 right shows, instead, that the Body Bending Energy (on y-axis) is much smaller than the Bending Energy calculated on the whole \mathbb{R}^m .

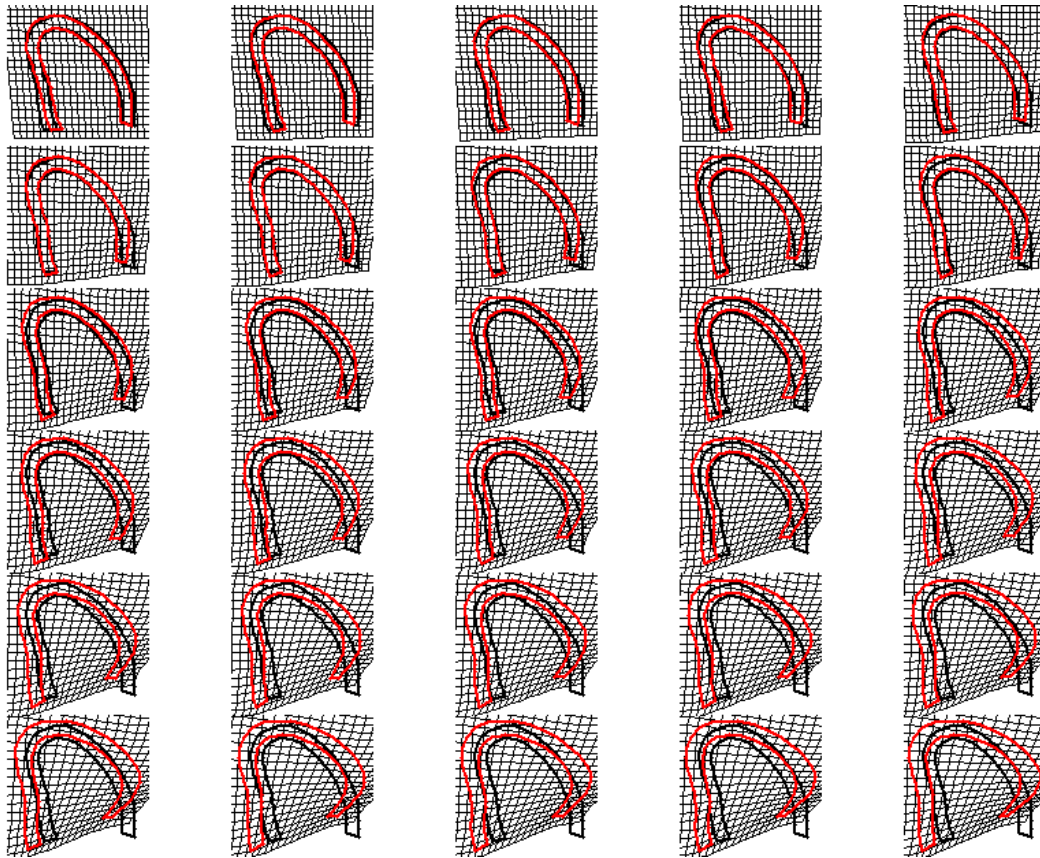


FIGURE 4 Simulated dataset with 30 shapes (red) that are deformation of the diastolic state of the healthy individuals (in black in each panel). Deformation grids were built using Thin Plate Spline.

Fig. 6 (top right) shows that the Γ -Energy calculated on original data between LOCS and their proper deformed states is perfectly conserved on transported data when computing it from CR. Fig. 6 (top left) shows also the non affine part of the Γ -Energy density that can be obtained by multiplying the Body Bending Energy density by the proper μ_2 coefficient for each deformed states. This part also is perfectly recovered by the TPS direct transport. Bottom side of Fig. 6 illustrates that neither the Bending Energy nor the Strain Energy are perfectly recovered. For the former case, in fact, Body Bending Energy is formally different from the Bending Energy. The Strain Energy density is not perfectly conserved as, being the real case not produced by parameterized bilinear transformations, it does not equate the Γ - Energy density. However, the deviation from isometry is not dramatic especially for the healthy individual (i.e. the black circles: Beta coefficient: 1.12).

Fig. 7 and 8 show the transformation grid of original data relatively to their proper LOC of the healthy and pathological subject respectively. Fig. 9 shows the transformation grids of transported data relatively to the chosen CR.

Fig. 10 shows the utility of a Parallel Transport. The upper panel shows the PCA space following a GPA: the PC1 explains the majority of variance and is related mainly to the difference between subjects, while the differences between deformations is relegated to the PC2 that explains a very small fraction of total variance. On the other hand, as shown in the bottom panel, after the use of TPS direct transport we can better appreciate the differences in deformation, i.e. magnitude, direction and size of the two trajectories. Deformation grids shows colour according to $\log(\det(I + \nabla u))$ coming from the two-dimensional Thin Plate Spline first derivative evaluated within the body. Negative values indicate that, with respect to the source (here the sample consensus in red), the target (here the PC's extremes in black) experiences a reduction in the local area, while values >0 indicate an enlargement.

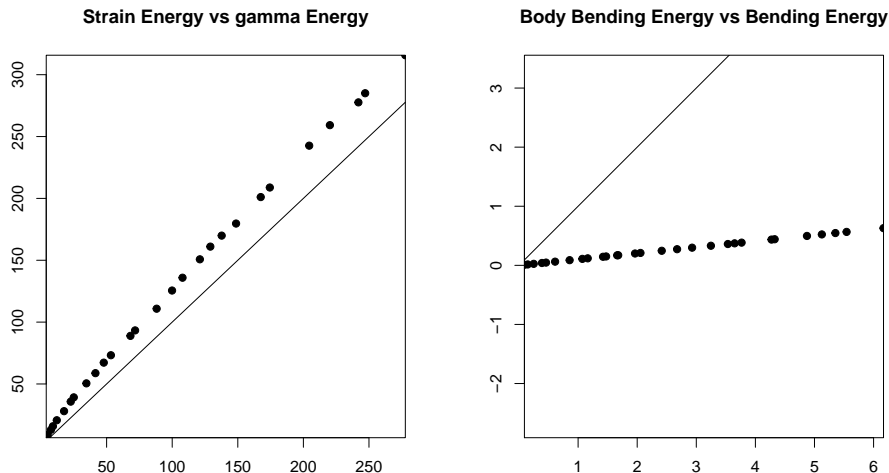


FIGURE 5 Comparison between different energies calculated using the simulated dataset illustrated in Fig. 3. Left: Strain Energy (on y-axis) vs. Gamma Energy (on x-axis). Right: Body Bending Energy (on y-axis) vs. Bending Energy (on x-axis).

6 | DISCUSSION AND CONCLUSIONS

We have shown that restricting the calculation of the bending energy to the body, instead using it calculated on the whole \mathbb{R}^m , allows us to tune the original TPS direct transport in order to conserve Γ -energy and Body bending energy densities. The body bending energy is estimated by building the corresponding BEB matrix that can be thought as a modification of the classic bending energy matrix but having the advantage that the physical non affine deformation of the body is now correctly captured within its real boundaries. This implementation of the original formulation of the TPS direct transport makes it particularly suitable in cases where the analysis of deformation is oriented to a mechanical interpretation of the phenomenon under study. We also stress that formulations presented here have been developed for 2D cases but they are extendable to three-dimensions in order to embrace a wider range of examples and to better approach reality for those studies that can exploit modern 3D imaging technologies.

7 | APPENDIX

In this section we summarize some basic algebraic operations used in the paper. In particular, let \mathcal{E}^m and $\mathcal{V}\mathcal{E}^m$ be the Euclidean space of dimension m and the related translation space, respectively. We identify $\mathcal{E}^m \equiv \mathcal{V}\mathcal{E}^m \equiv \mathbb{R}^m$ through the choice of an origin o and a orthonormal basis e_1, \dots, e_m . Each vector $v \in \mathbb{R}^m$, can be represented as:

$$v = v_i e_i = (v_1, \dots, v_m)^T$$

where $i = 1 \dots m$ and summation convention over repeated indexes is employed. The dot product between two vectors $u, v \in \mathbb{R}^m$ is then defined as:

$$u \cdot v = u_\alpha v_\alpha$$

A second order tensor is a linear map on $\mathcal{V}\mathcal{E}^m$; the dot product between two second order tensors $A, B \in \mathbb{R}^{(m \times m)}$ is defined as:

$$A \cdot B = Tr(A^T B)$$

We can define second order tensors by composing two vectors through a tensor product; by definition, the tensor product of $a, b \in \mathbb{R}^m$ is the linear map on $\mathcal{V}\mathcal{E}^m$; defined by:

$$(a \otimes b)u = a(b \cdot u), \text{ with } u \in \mathbb{R}^m$$

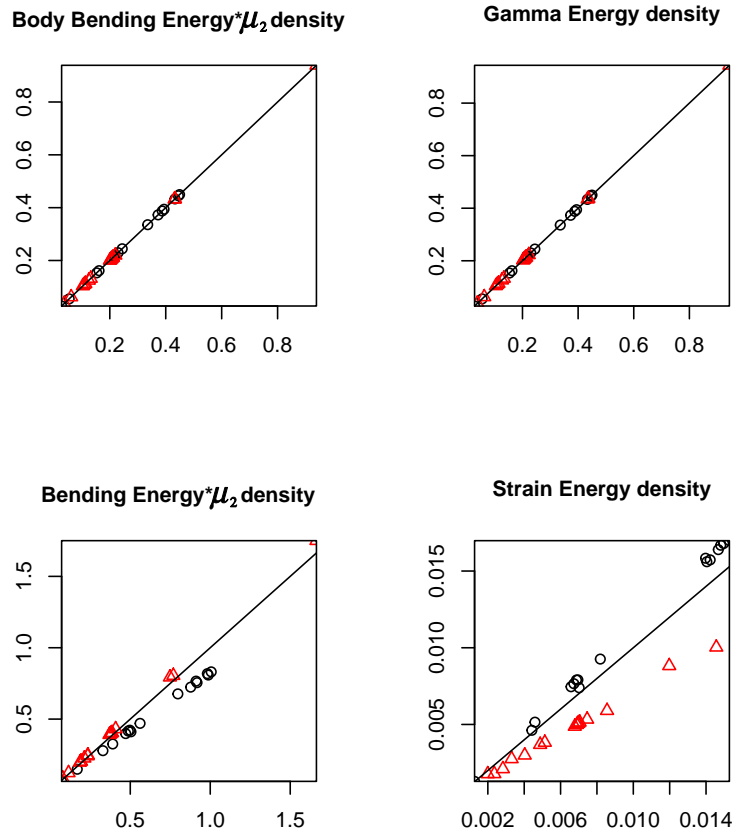


FIGURE 6 Energy densities computed after the TPS Direct Transport procedure (on y-axis) between the Common Reference and transported data contrasted with the Energy densities calculated on original data between the corresponding per-group local references and their proper deformed states (on x-axis). Black circles indicate the healthy individuals while red triangles the pathological one.

In the same way the tensor product between three vectors $a, b, c \in \mathbb{R}^m$ is a third order tensor, here defined by means of its action on a fourth vector $u \in \mathbb{R}^m$:

$$(a \otimes b \otimes c)u = (a \otimes b)(c \cdot u)$$

References

1. Maiorino L, Farke A, Kotsakis T, Piras P. Is Torosaurus Triceratops? geometric morphometric evidence of late Maastrichtian ceratopsid dinosaurs. *PLoS ONE* 2013; 8(11). doi: 10.1371/journal.pone.0081608
2. Piras P, Teresi L, Buscalioni A, Cubo J. The shadow of forgotten ancestors differently constrains the fate of Alligatoroidea and Crocodyloidea. *Global Ecology and Biogeography* 2009; 18(1): 30-40.
3. Piras P, Buscalioni A. *Diplocynodon muelleri* comb. nov., an Oligocene diplocynodontine alligatoroid from Catalonia (Ebro Basin, Lleida Province, Spain). *Journal of Vertebrate Paleontology* 2006; 26(3): 608-620.
4. Piras P, Evangelista A, Gabriele S, et al. 4D-analysis of left ventricular heart cycle using Procrustes motion analysis. *PLoS one* 2014; 9(1): e86896.

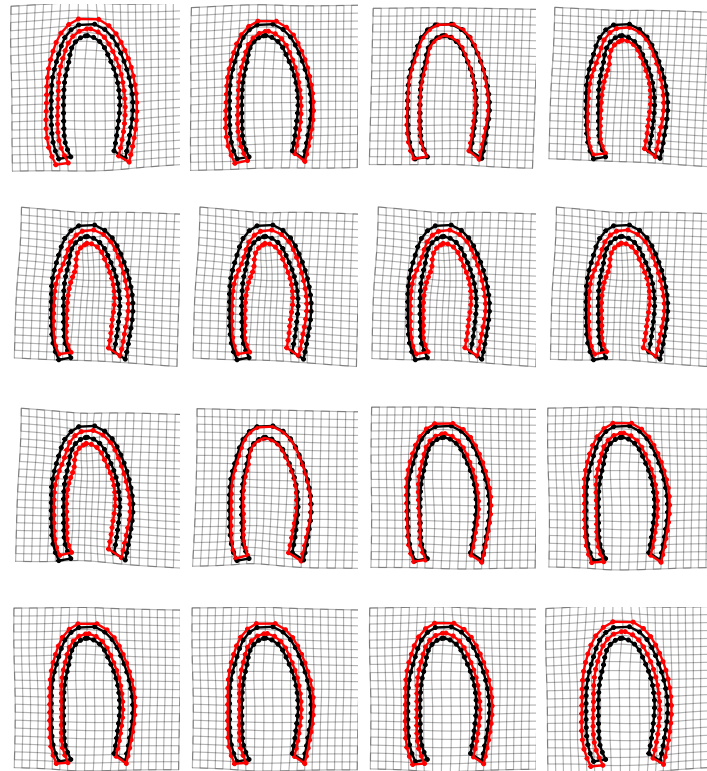


FIGURE 7 TPS deformation grids for the healthy individual computed from the healthy heart cycle' Grand Mean.

5. Pokrass J, Bronstein A, Bronstein M. Partial shape matching without point-wise correspondence. *Numerical Mathematics* 2013; 6(1): 223-244.
6. Cosmo L, Rodolà E, Bronstein MM, Torsello A, Cremers D, Sahillioğlu Y. Partial Matching of Deformable Shapes. In: 3DOR '16. Eurographics Association; 2016; Goslar Germany, Germany: 61-67.
7. Miller MI, Qiu A. The emerging discipline of computational functional anatomy. *Neuroimage* 2009; 45(1): S16-S39.
8. Miller MI, Younes L, Trouvé A. Diffeomorphometry and geodesic positioning systems for human anatomy. *Technology* 2014; 2(01): 36-43.
9. Miller M, Trouvé A, Younes L. Hamiltonian Systems and Optimal Control in Computational Anatomy: 100 Years since D'Arcy Thompson. *Annual Review of Biomedical Engineering* 2015; 17: 447-509.
10. Varano V, Gabriele S, Teresi L, et al. Comparing shape trajectories of biological soft tissues in the size-and-shape space. In: ; 2015: 351-365.
11. Milicchio F, Varano V, Gabriele S, Teresi L, Puddu P, Piras P. Parallel transport of local strains. *Computer Methods in Biomechanics and Biomedical Engineering: Imaging & Visualization* 2018.
12. Varano V, Gabriele S, Teresi L, et al. The TPS Direct Transport: a new method for transporting deformations in the Size-and-shape Space. *International Journal of Computer Vision* 2017.
13. Varano V, Piras P, Gabriele S, et al. The decomposition of deformation: New metrics to enhance shape analysis in medical imaging.. *Medical Image Analysis* 2018; 46: 35-56. doi: 10.1016/j.media.2018.02.005

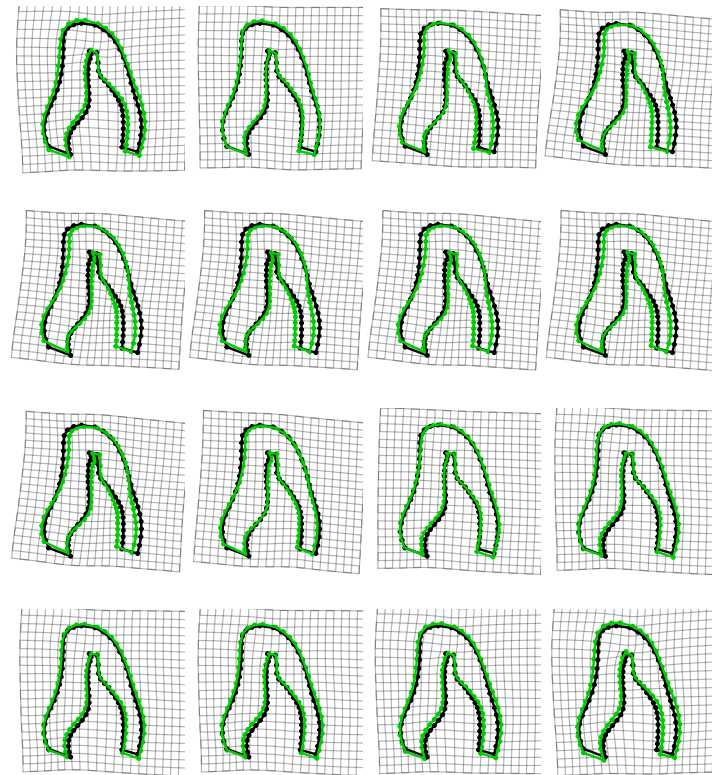


FIGURE 8 TPS deformation grids for the pathological individual computed from the pathological heart cycle' Grand Mean.

14. Dryden IL, Mardia KV. *Statistical Shape Analysis, with Applications in R. Second Edition*. Chichester: John Wiley and Sons . 2016.
15. Bookstein FL. Principal warps: Thin-plate splines and the decomposition of deformations. *IEEE Transactions on pattern analysis and machine intelligence* 1989; 11(6): 567–585.
16. Kent JT, Mardia KV. *The Link Between Kriging and Thin-plate Splines*. 24; 1994.
17. Younes L. *Shapes and diffeomorphisms*. 171. Springer Science & Business Media . 2010.
18. Piras P, Teresi L, Gabriele S, et al. Systo-diastolic LV shape analysis by geometric morphometrics and parallel transport highly discriminates myocardial infarction. *Lecture Notes in Computer Science (including subseries Lecture Notes in Artificial Intelligence and Lecture Notes in Bioinformatics)* 2016; 9534: 119-129.
19. Piras P, Torromeo C, Re F, et al. Left Atrial trajectory impairment in Hypertrophic Cardiomyopathy disclosed by Geometric Morphometrics and Parallel Transport. *Scientific Reports* 2016; 6.
20. Madeo A, Piras P, Re F, et al. A new 4D trajectory-based approach unveils abnormal LV revolution dynamics in hypertrophic cardiomyopathy. *PloS one* 2015; 10(4): e0122376.
21. Piras P, Torromeo C, Evangelista A, et al. Homeostatic Left Heart integration and disintegration links atrio-ventricular covariation's dyshomeostasis in Hypertrophic Cardiomyopathy. *Scientific Reports* 2017; 7(1).
22. Evangelista A, Gabriele S, Nardinocchi P, et al. Non-invasive assessment of functional strain lines in the real human left ventricle via speckle tracking echocardiography. *Journal of biomechanics* 2015; 48(3): 465–471.

23. Gabriele S, Nardinocchi P, Varano V. Evaluation of the strain line patterns in a human left ventricle: a simulation study. *Computer Methods in Biomechanics and Biomedical Engineering* 2015; 18(7): 790-798.
24. Gabriele S, Teresi L, Varano V, et al. On the strain line patterns in a real human left ventricle. In: ; 2014: 19-24.



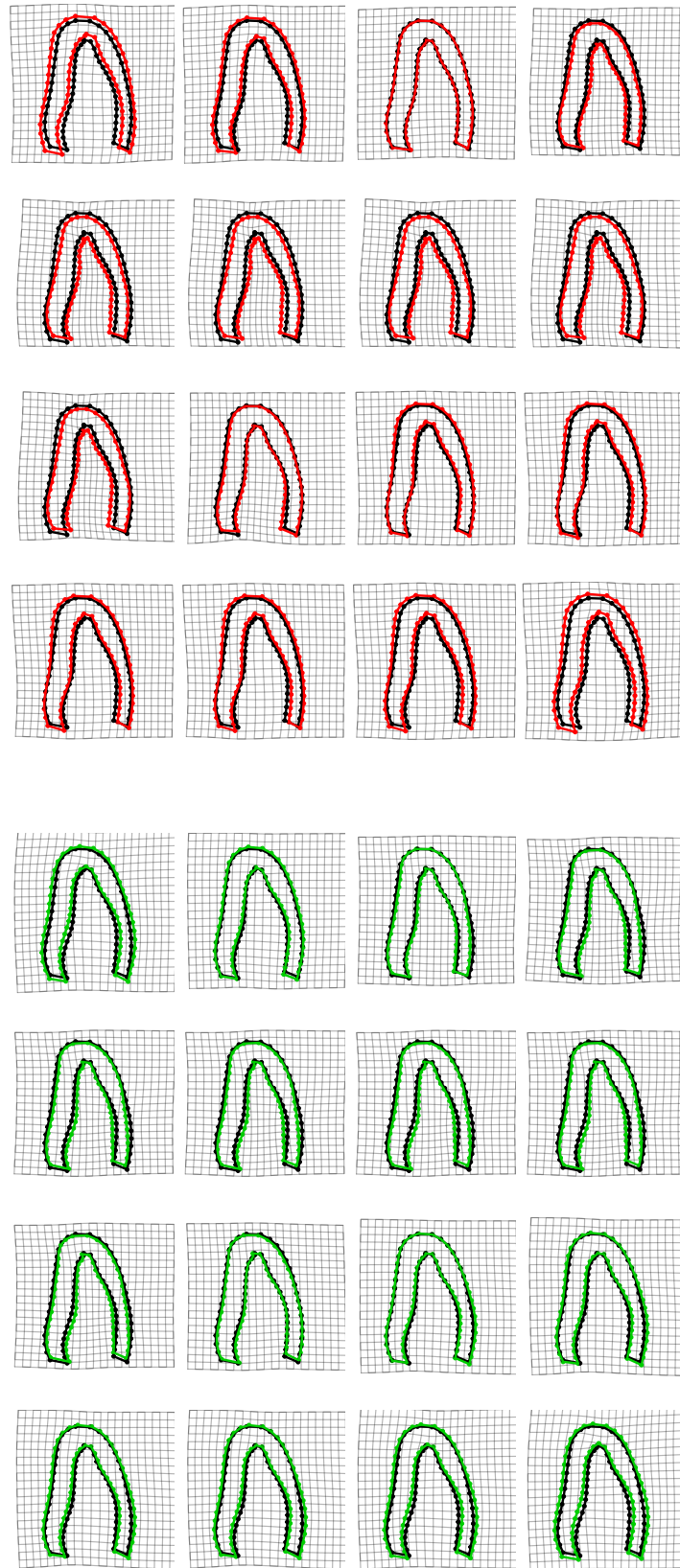


FIGURE 9 TPS deformation grids for the transported data computed from the chosen Common Reference toward which deformation were transported.

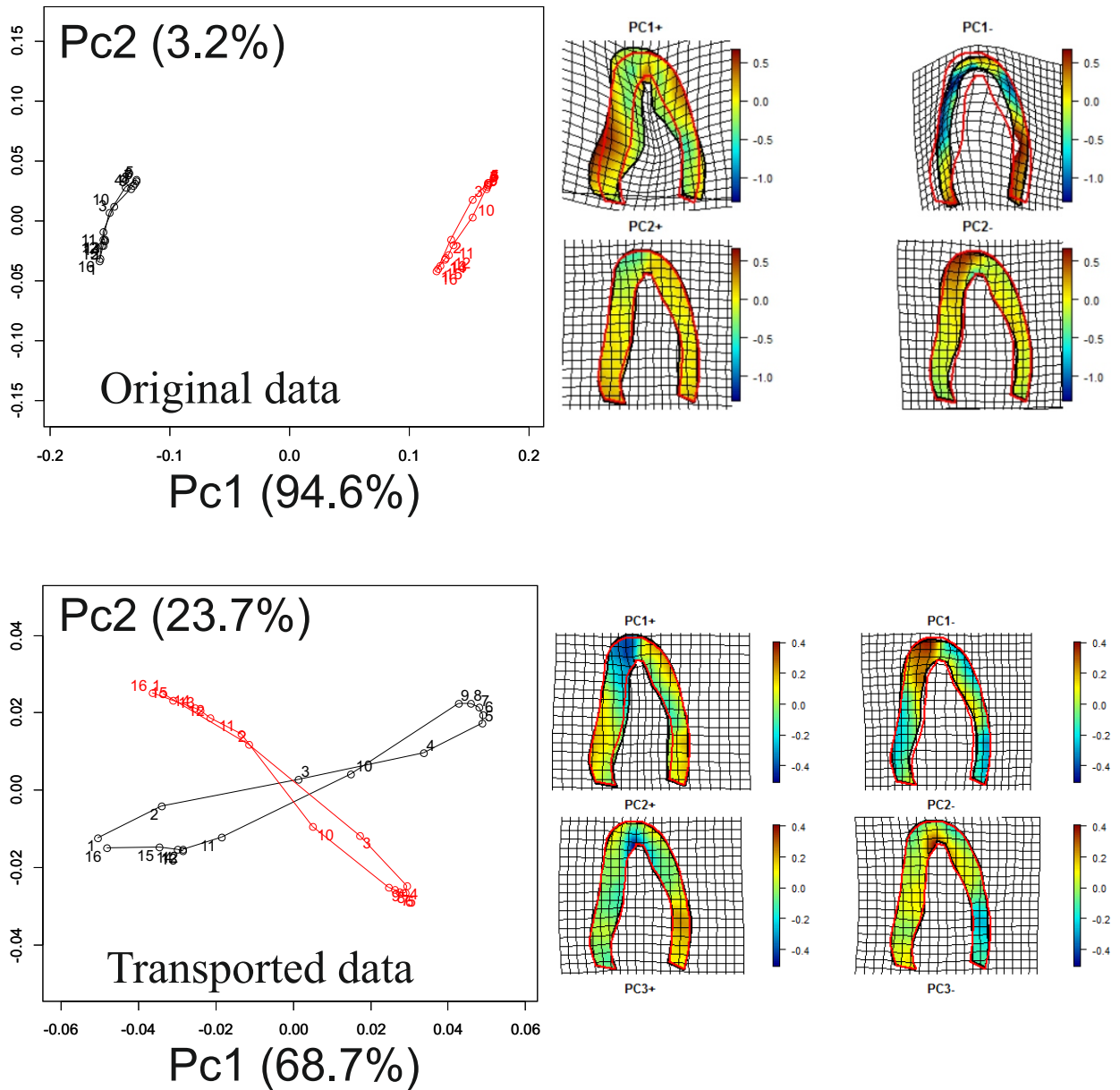


FIGURE 10 PCA and deformations associated to PC axes' extremes computed on original data (upper panel) and on transported data (lower panel). Deformation grids shows color according to $\log(\det(I + \nabla u))$ coming from the two-dimensional Thin Plate Spline first derivative evaluated within the body. Values <0 indicate that, with respect to the source (here the sample' consensus in red), the target (here the PC's extremes in black) experiences a reduction in the local area, while values >0 indicate an enlargement.